Materials Research Proceedings 54 (2025) 448-457 https://doi.org/10.21741/9781644903599-49

Prediction quality of macroscopic forming simulation of non-crimp fabrics for aerospace applications

Jan Paul Wank[1,a*], Stefan Haas[2], Dominik Dörr[2], Patrik Runeberg[3], Benedikt Lux[3], Constantin Krauß[1], Bastian Schäfer[1] and Luise Kärger[1,b]

[1]Karlsruhe Institute of Technology (KIT), Institute of Vehicle System Technology (FAST) – Lightweight Engineering, Rintheimer Querallee 2, 76131 Karlsruhe, Germany

[2]Simutence GmbH, Rintheimer Querallee 2, 76131 Karlsruhe, Germany

[3]Airbus GmbH (formerly Premium Aerotec GmbH), Haunstetter Straße 225, 86179 Augsburg, Germany

[a]jan.wank@kit.edu, [b]luise.kaerger@kit.edu

Keywords: Non-Crimp Fabric, Forming, Process Simulation

Abstract. A fully automated resin transfer molding (RTM) process is commonly used to manufacture large quantities of continuous fiber-reinforced composite components economically. Due to the high cost of process development, the process is currently used only to a limited extent in aerospace applications. Virtual process chains significantly reduce the process development phase. The simulation of the individual process steps enables the virtual safeguarding of the manufacturability of components and systems. The first step in the process simulation of the RTM process is forming. Compared to woven fabrics, the modeling of non-crimp fabrics (NCFs) at the macroscopic simulation level is not yet sufficiently established. Therefore, this work investigates the predictive quality of the current forming simulation methods for NCFs. The geometry of the validation component is derived from an aerospace application. A segmented stamp concept is developed to mitigate forming defects. First, the stamp concept is virtually optimized by adjusting the segmentation and sequence. Second, the optimized tooling concept is manufactured, and experimental forming studies are performed. Finally, the simulation results and the produced preforms are compared to demonstrate the predictive quality of current simulation models for NCF forming.

Introduction

The aerospace industry places considerable significance on utilizing lightweight construction as a fundamental design principle. Fiber-reinforced plastics are becoming increasingly prevalent due to their high weight-specific stiffness and strength. The deployment of fiber-reinforced composites enables weight savings of up to 40% for secondary structures and up to 20% for primary structures compared to light metal alloys in aerospace applications [1].

The process of autoclaving has long been established as a means of producing fiber-reinforced components within the aerospace industry. However, the process is characterized by long cycle times, high costs for the prepreg materials, and the necessity for specialized storage conditions [2]. As a result, the resin transfer molding (RTM) process has recently been investigated for use in the aerospace industry. The RTM process uses dry textiles, which are less expensive than prepregs and do not require special storage conditions. In the first stage of the RTM process, semi-finished textiles are draped into a preform. In the second stage, the preform is infiltrated with the reactive polymer matrix. The curing of the composite begins after the impregnation of the matrix. Once cured, the part can be demolded. The preform can be produced in batches and stored until the infiltration is performed. The RTM process is highly automatable and requires minimal manual labor compared to autoclave processes, allowing for high production rates [3]. The closed tool of

the RTM forming and infiltration stages results in excellent surface quality, but also high tooling costs [3].

In the context of dry semi-finished products employed in the RTM process, non-crimp fabrics (NCFs) exhibit a different fiber architecture than woven fabrics, given that the fiber rovings are held together extrinsically by stitching. As a result, the fibers are aligned straight and display no out-of-plane undulations, resulting in higher lightweight potential than woven fabrics. An advantage of bidirectional (BD) NCFs compared to unidirectional (UD) composites is that multiple orientations can be combined in a single layer. This results in a more efficient and consequently more economical production of preforms, as a multiaxial semi-finished product can be deposited in a single axis in one production step [2].

Within an industrial context, a continuous CAE chain is an efficient tool for integrated product development [4]. The individual process steps are modeled virtually, and the results are transferred to downstream simulation steps via suitable interfaces. Virtual optimization can significantly reduce the tooling's development costs and process development phase.

Constitutive laws that accurately describe the material's behavior are needed to predict manufacturing effects in process simulations. Developing simulation models at the macroscopic level is an essential requirement for efficiently simulating technically relevant components. While macroscopic methods for woven fabrics are already state of the art [5–9], such methods have yet to be established for NCF. Most simulations of NCF have been conducted at the mesoscopic level, where the fibers and the stitching are depicted discreetly [10–13]. More recently, NCF models have also been developed at the macroscopic level [14–17]. To model the relevant forming mechanisms, it is necessary for macroscopic approaches to capture mesoscopic effects in a homogenized form.

This study outlines a forming simulation workflow for the RTM process. A component derived from an aerospace application is utilized as a demonstrator, comprising 16 layers of uni- and bidirectional NCF, including four local patch reinforcements. In this context, the material models used to model the forming behavior of NCF are presented. The NCF material is experimentally characterized, and the material model is subsequently parameterized. The tool's stamp concept is then optimized virtually. Based on the stamp concept, the tool is manufactured, and preforms are produced. Finally, the results of the forming simulation and the preforms are compared to evaluate the current level of predictive quality of the proposed NCF forming simulation model.

Material modeling for uni- and bidirectional non-crimp fabrics

The following paragraphs list the applied approaches for describing the membrane, bending, and interface behavior. The methods are implemented via user subroutines in the commercial Finite Element (FE) solver ABAQUS/EXPLICIT.

Membrane behavior. The material model was initially proposed by Schäfer et al. [17] for unidirectional NCFs. Additionally, Schäfer et al. examined the transferability of the model to bidirectional NCFs [18]. The potential and limitations of the model for the application to a 0°/90° bidirectional NCF are investigated in an additional publication [19].

The material model is based on a hyperelastic approach. In hyperelastic approaches, the strain energy density W_{tot} is defined as a stress potential. For an anisotropic hyperelastic material the strain energy density can be described by directional pseudo-invariants I_i $(i = 4, 6, 8, 11)$. The pseudo-invariants describe the properties of the fiber families and their interaction with other material parameters. To relate them to the observed deformation modes of the material, the pseudo-invariants are chosen based on the principal material orientations. For the second Piola-Kirchhoff stress tensor $\boldsymbol{S}$, the following relationship (Eq. 1) applies:

$$S = 2\frac{\partial W_{\mathrm{tot}}(\boldsymbol{C})}{\partial \boldsymbol{C}} = 2\sum_i^N \frac{\partial W_{\mathrm{tot}}(I_i)}{\partial I_i}\frac{\partial I_i}{\partial \boldsymbol{C}} \tag{1}$$

with the right Cauchy-Green tensor $\boldsymbol{C}$. The deformation modes are often assumed to be independent of each other. Thus, the deformation energy density can be decomposed additively, and each component, quantified by a pseudo-invariant, correlates with a deformation mode. The typical deformation modes of UD-NCF are tension in the fiber direction (I_4), transverse tension (I_8), shear deformation (I_6) and in-plane compression perpendicular to the rovings (I_{11}). UD-NCFs deform under large shear strains, superimposed by transverse tensile deformation and in-plane compression perpendicular to the fiber orientation. Therefore, UD-NCFs are subjected not only to pure or simple shear but also to mixed deformation modes. In areas of high roving compression, there is significant roving slippage compared to cases where the tension of the stitching limits the shear deformation. To adequately model this interaction, a coupling between the transverse tension of the stitching (I_8) and perpendicular compression (I_{11}) is introduced. The strain energy density is given by Eq. 2:

$$W_{\mathrm{tot}}^{\mathrm{UD}}(I_4, I_6, I_8, I_{11}) = W_4^{\mathrm{UD}}(I_4) + W_6^{\mathrm{UD}}(I_6) + W_8^{\mathrm{UD}}(I_8, I_{11}) + W_{11}^{\mathrm{UD}}(I_{11}). \quad (2)$$

In contrast to UD-NCFs, bidirectional NCFs with perpendicular fiber directions display a shear-dominated membrane behavior, which can be asymmetric based on the stitching pattern and its orientation. Based on these observations, a simplified shear-based approach is proposed. The roving slippage is neglected, and only the stress in both roving directions, the pure shear, and the tension of the stitching (I_{stitch}), are considered. This yields the strain energy density for bidirectional NCFs as follows (Eq. 3):

$$W_{\mathrm{tot}}^{\mathrm{BD}}(I_4, I_6, I_8, I_{\mathrm{S}}) = W_4^{\mathrm{BD}}(I_4) + W_6^{\mathrm{BD}}(I_6) + W_8^{\mathrm{BD}}(I_8) + W_{\mathrm{stitch}}^{\mathrm{BD}}(I_{\mathrm{stitch}}). \quad (3)$$

The material model is implemented in a user material subroutine for ABAQUS/EXPLICIT (VUMAT). The subroutine is applied to M3D3 membrane elements whose edges are aligned with the fiber direction to circumvent numerical intra-ply locking [20]. For a comprehensive description of the material law, the definition of the pseudo-invariants, and the coupling introduced for UD-NCF, the reader may refer to Schäfer et al. [17].

Bending behavior. The approach used to describe the bending behavior [21] has already been used for UD-NCF [14] and can also be applied to bidirectional fabrics. Due to the low transverse stiffness of dry textiles, the bending behavior during forming must be considered decoupled from the membrane behavior. The bending behavior is described by a hypoelastic material law to account for large shear deformations. A linear-elastic orthotropic bending stiffness in the non-orthogonal fiber-parallel material system is considered. The approach is implemented in a user subroutine VUGENS, which handles the thickness integration scheme for the linear triangular shell elements (S3R). For the decoupling of membrane and bending behavior, the membrane and shell elements are superimposed via shared nodes.

Interface behavior. The inter-ply deformation behavior includes the tool-ply interface and the ply-ply interface. For the forming simulation, tangential sliding between the two interfaces is assumed. It is based on Coulomb's law of friction. The built-in ABAQUS/EXPLICIT general contact algorithm is used for the contact.

Material characterization and parameterization

The following section presents the respective coupon tests conducted to characterize the material. Inverse parameterization from the simulation of the coupon tests is employed for the membrane and bending behavior.

Three NCF materials are selected for consideration in the forming simulation. The NCFs include a UD-NCF, a bidirectional NCF with 0°/90° fiber orientation (BD-NCF 0/90), and a BD-NCF +45/-45, as illustrated in Fig. 1. The fibers are high-tensile-strength carbon fibers and the

stitching is polyester yarn. A powder binder based on a heat-activated epoxy is applied to the top of the dry textiles to facilitate the handling of the produced preforms.

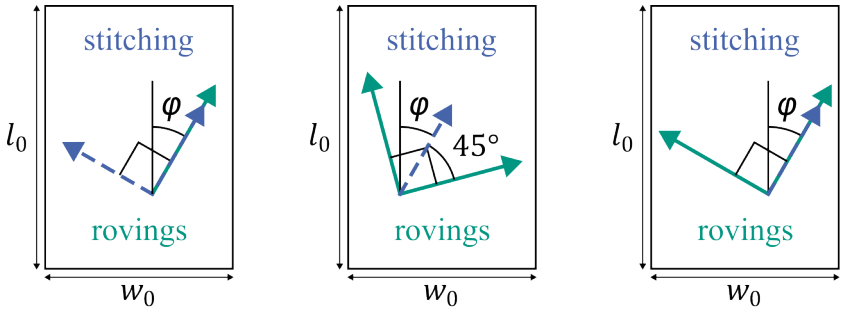

a) UD-NCF b) BD-NCF +45/-45 c) BD-NCF 0/90

Figure 1 – Fiber architecture showing the stitching and roving direction of the used NCFs. The 0°-direction for the off-axis tensile tests follows for $\varphi = 0°$.

Membrane. Off-axis tensile (OAT) tests are used to characterize the membrane behavior, cf. Fig. 1. A standardized tensile testing machine is employed for this purpose. A specialized clamping device prevents the samples from slipping [14]. Three OATs with angles φ of 30°, 45° and 60° are carried out as part of the investigation for the UD-NCF. In the case of the BD-NCF +45/-45, the angles φ are 0° and 90°, while for the BD-NCF 0/90, they are 45° and 135°. The specimens have an aspect ratio of $a = l_0/w_0 = 2$, where l_0 is the initial height and w_0 is the initial width. The force-displacement curves for the OAT tests of the BD-NCF are illustrated in Fig. 2. The stitching does not significantly impact the membrane behavior of the BD-NCF 0/90, which falls within the standard deviation (Fig. 2a). As illustrated in Fig. 2b, the stitching considerably influences the membrane behavior under tension for the BD-NCF +45/-45. The two BD-NCFs exhibit different shear behaviors. The UD-NCF displays the anticipated behavior, so reference is made here to Schäfer et al. [22].

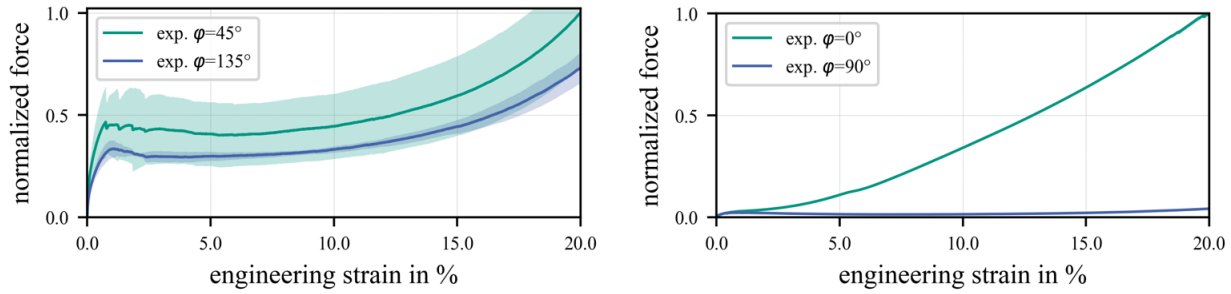

a) BD-NCF 0/90 b) BD-NCF +45/-45

Figure 2 – Force-engineering strain curves from the OAT tests for both BD-NCFs (normalized to the respective maximum force values).

The material model is parametrized based on the forces and strains measured in multiaxial deformation states from all the OATs outlined above in Fig. 2 for the corresponding NCFs. The parameters characterizing the membrane behavior are identified using an FE model and an inverse optimization procedure. Fig. 3 illustrates the force-displacement curves resulting from the simulation for the final parameterization of the BD-NCF 0/90 $\varphi = 135°$ and the BD-NCF +45/-45 $\varphi = 90°$, which are compared with the corresponding experimental curves. The determined force-displacement curves show good overall agreement with the experimental data. The initial increase in stiffness can be attributed to the applied powder binder, which cannot be reproduced with the current modeling approach. The parameterization of the UD-NCF follows analogously and is not discussed further.

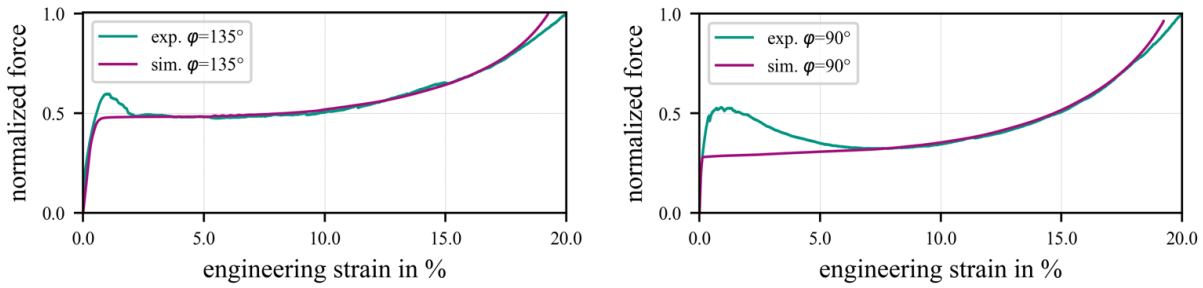

a) BD-NCF 0/90 b) BD-NCF +45/-45

Figure 3 – Force-engineering strain ratio curves, including the experimental and fitted results (normalized to the respective maximum force values).

Bending. The cantilever test ASTM D1388-18 standard [23] is employed to determine the elastic bending modulus of NCFs. The tests are carried out with a binder at the top and bottom. The determined bending stiffness allows the conclusion that the binder has no significant influence on the bending properties of the NCFs. The material parameters of the bending behavior are identified inversely using an FE model.

Interface. Friction tests are conducted to characterize the tool-ply and ply-ply friction behavior. To this end, a standard tensile test setup is connected to a friction test rig that was developed following the ASTM D1894-14 standard [24]. Different friction partners are investigated, and the respective mean value of the determined tool-ply and ply-ply friction coefficients is applied.

Workflow of the draping simulation

The geometry and laminate layup of the preform are predefined boundary conditions due to the targeted application. The geometry is illustrated in Fig. 4. The laminate layup comprises 16 layers of UD- and BD-NCFs and an additional four patches for local reinforcement. The patches are the first four layers starting from the bottom of the layup. The first complete ply and the top ply is a BD-NCF +45/-45. The tight radius and the double curvature within it, as illustrated in Fig. 4a, make the forming of the component a challenging task that requires a customized, segmented stamp concept. Initial hand-drawn forming trials identified the area of the double curvature as a critical area for forming.

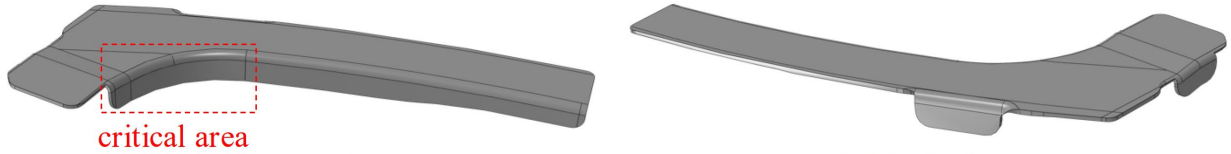

a) Front view b) Back view

Figure 4 – Part geometry of the considered component.

The FE model of the tool and the semi-finished textile product are generated automatically using an ABAQUS/CAE plugin, available under the name SimuDrape [25]. The tools are modeled as rigid bodies. The decoupling of the membrane and bending behavior is achieved by superimposing M3D3 and S3R elements with shared nodes for each NCF ply. The discretization is carried out with an edge length of 5 mm, which corresponds to the width of the rovings. An alignment of the element edges along the fiber orientations is necessary to avoid tension locking [20].

Stamp concept. The segmented stamp concept, which comprises eight independently moving stamps, is illustrated in Fig. 5.

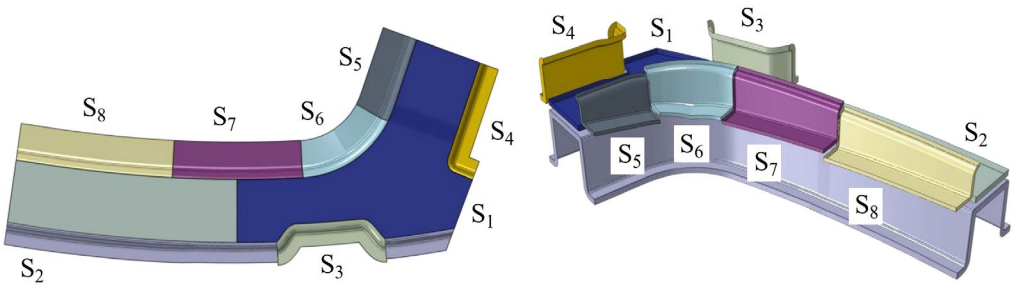

a) Top view b) Front view

Figure 5 – Tooling with the segmented stamp concept used for draping.

The stamp profile is arranged so that the two blank holder stamps S_1 and S_2 move first. The two hold-down stamps compress the laminate layup and move lower than the final cavity height. As a result, the stack is fixed during further forming, preventing it from slipping out of the mold. Stamps S_3, S_4, and S_6 start moving simultaneously but with different displacement profiles. Punch S_6 is provided with a wedge geometry, whereby the wedge tip is in the middle of the radius of the double curvature. The stamps S_5, S_7, and S_8 are slanted. In combination with the associated displacement profiles, a continuous forming slope of the stamps is obtained during the process. This causes the stack to be driven outward from the critical radius. Using a BD-NCF 0/90 layer as an example, Fig. 6 shows that the number of wrinkles and shear bands is significantly reduced due to the continuous forming slope compared to standard planar stamps.

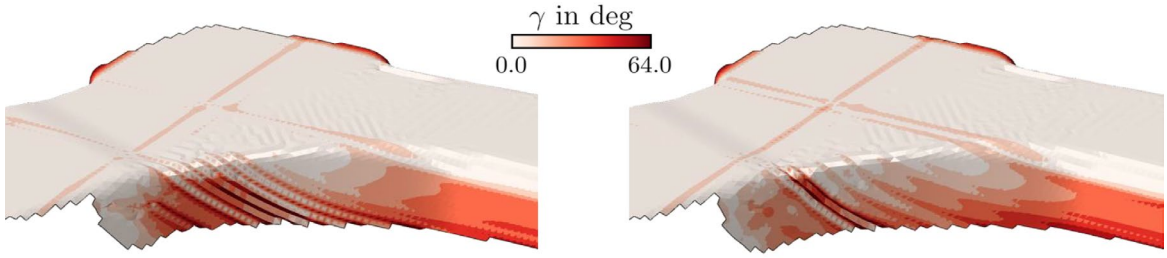

a) Standard stamp concept b) Slanted stamp concept

Figure 6 – Comparison of the shear angle distribution γ for the stamp concepts with standard and slanted stamps for a BD-NCF 0/90 plie.

Area-locking function. The evaluation of the simulation results showed that in the BD-NCF +45/-45 plies an unphysical shearing of the elements occurs because the element area is not limited to its physical maximum (see Fig. 7a). This is due to the component radius and the fact that the fiber rovings span across the radius from one side to the other side. To limit this to a physical degree, a locking function is introduced based on the fiber volume content V_f and the element area A because the elements are two-dimensional. The initial fiber volume content in the undeformed configuration A_0 for the targeted cavity height is assumed to be $V_{\mathrm{f},0} = 0.6$ and the maximum packing density is assumed to be $V_{\mathrm{f,max}} = 0.907$. These values result in the physically minimum possible element area A_{min}. Using a smooth step function, the material is artificially stiffened if the element area exceeds the values $A \geq A_{\mathrm{min}}$ and $A < A_0$ by adding a numerical locking stiffness E_{locSurf}. To stay within the scope of the energy formulation of Eq. 1, the artificial contribution is connected to the invariant $\sqrt{\det(\boldsymbol{C})}$. Fig. 7b shows that the artificial stiffening reduces the material draw-in and reduces the shear angle. At the same time, wrinkling occurs in the flat areas outside the radius due to the reduced shearability of the material.

Materials Research Proceedings 54 (2025) 448-457 https://doi.org/10.21741/9781644903599-49

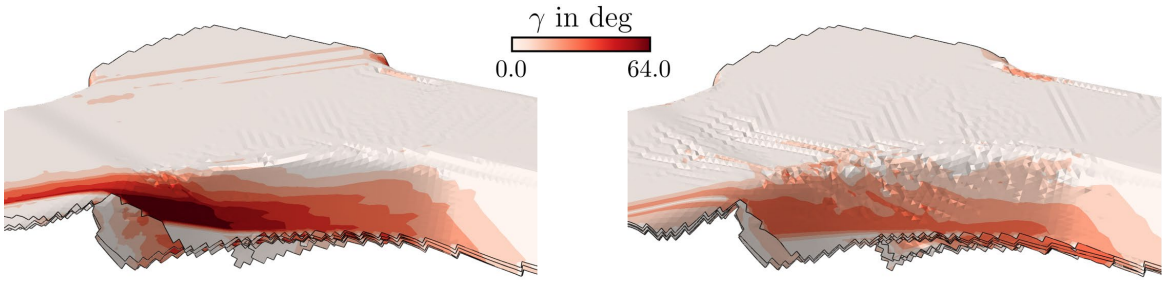

a) Without area-locking b) With area-locking

Figure 7 – Comparison between the material draw-in for the top BD NCF +45/-45 ply without and with the new area-locking function.

Comparison of simulation results and preform

The tooling was manufactured based on the virtually developed stamp concept. In the following, the simulation results are qualitatively compared with the manufactured preforms. The top and bottom layers, both BD-NCF +45/-45, are evaluated in detail.

The top view comparison is shown in Fig. 8. In the red areas, wrinkles form in both the simulation and the preform that extend almost entirely across the component's width. In the green area, shear deformation is predicted. This shear deformation is due to the part's geometry because the rovings to the right of the green area are not pulled over the edge into the radius like the rovings on the left. The blue marking shows the material draw-in of the top layer, which is well predicted in the simulation. This draw-in indicates that the area-locking function is a necessary extension of the membrane behavior. In the simulation results in Fig. 8a, the patch plies located on the bottom of the layup are emerging from under the top layers (cf. yellow marking). This behavior is not observed in the preform in Fig. 8b. The inaccurate prediction of ply-ply behavior is due to the assumption of simple Coulomb friction between the plies and the neglect of the binder behavior.

The bottom view is shown in Fig. 9. Analogous to the top BD-NCF +45/-45 ply, the material draw-in from the bottom BD-NCF +45/-45 ply is well predicted (cf. green area in Fig. 9). In both the simulation and the preform, wrinkles appear in the blue area. While wrinkles are predicted in the orange area in the simulation, they do not occur in the preform. Similarly, the behavior of the patches seen in the simulation is also not seen in the preform for the reasons mentioned above (cf. yellow area in Fig. 9). In the area marked in red, a severe wrinkle, which is completely folded over, can be seen in the simulation as well as experimental results.

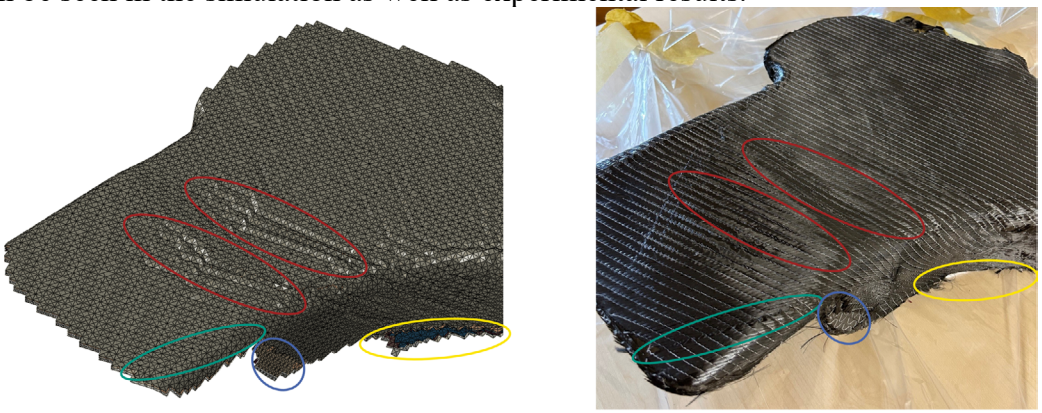

a) Simulation b) Preform

Figure 8 – Top view comparison between simulation results and preform with highlighted areas of interest.

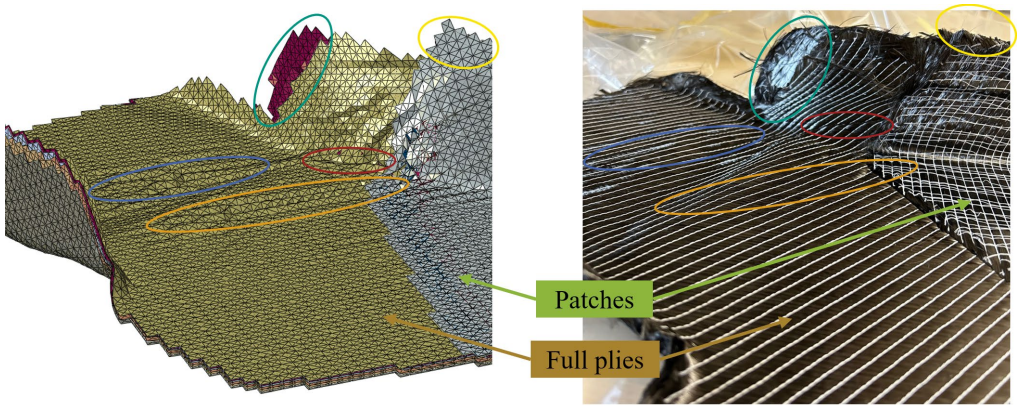

a) Simulation b) Preform

Figure 9 – Bottom view comparison between simulation results and preform with highlighted areas of interest.

Conclusion

The general workflow for setting up and carrying out a forming simulation for a complex geometry in aerospace applications was presented. The material models for membrane, bending, and interface behavior were introduced with a focus on describing the deformation behavior of BD-NCFs. The characterization of the NCF material and the subsequent parameterization of the material models were described. The advantages of the segmented stamp concept were demonstrated. By establishing a continuous forming slope, the occurrence of wrinkles in the critical area was significantly reduced. The unphysical shear of the elements due to the geometry and layup constraints was reduced by introducing an area-locking function. The material was artificially stiffened based on the theoretical fiber volume content. The area-locking function improved the prediction accuracy regarding wrinkle location and material draw-in. Finally, the manufactured preforms and the simulation results were qualitatively compared. The comparison shows that with the current state of NCF forming simulation, a large number of relevant forming defects such as material draw-in, the occurrence and severity of wrinkles can already be predicted with good agreement between simulation and reality. This is why NCF forming simulations can already be a valuable tool for process development and resource conservation.

Acknowledgement

The authors would like to thank the German Federal Ministry for Economic Affairs and Climate Action (BMWK) for funding the LuFo research project Electra (20W1912D), for which the work has been carried out. This work is also part of the Heisenberg project 'Digitalization of fiber-reinforced polymer processes for resource-efficient manufacturing of lightweight components', funded by the DFG (project no. 455807141). In this work, the SimuDrape add-on was used to create the simulation model in ABAQUS/EXPLICIT. The presented approach for NCF modeling has recently been made available in the Abaqus add-on SimuDrape [25].

References

[1] P. Irving, C. Soutis, Polymer composites in the aerospace industry, Woodhead Publishing, 2019. https://doi.org/10.1016/C2017-0-03502-4

[2] M.A. Lepore, L. Ferrante, L. Sanguigno, A.R. Maligno, A non-crimp fabric mechanical characterization for the production of aerospace components, Material Design & Processing Communications 3 (2021) e222. https://doi.org/10.1002/mdp2.222

[3] M. Bodaghi, R. Costa, R. Gomes, J. Silva, N. Correia, F. Silva, Experimental comparative study of the variants of high-temperature vacuum-assisted resin transfer moulding, Composites

Part A: Applied Science and Manufacturing 129 (2020) 105708. https://doi.org/10.1016/j.compositesa.2019.105708

[4] L. Kärger, S. Galkin, C. Zimmerling, D. Dörr, J. Linden, A. Oeckerath, K. Wolf, Forming optimisation embedded in a CAE chain to assess and enhance the structural performance of composite components, Composite Structures 192 (2018) 143–152. https://doi.org/10.1016/j.compstruct.2018.02.041

[5] M.A. Khan, T. Mabrouki, E. Vidal-Sallé, P. Boisse, Numerical and experimental analyses of woven composite reinforcement forming using a hypoelastic behaviour. Application to the double dome benchmark, Journal of Materials Processing Technology 210 (2010) 378–388. https://doi.org/10.1016/j.jmatprotec.2009.09.027

[6] M. Machado, M. Fischlschweiger, Z. Major, A rate-dependent non-orthogonal constitutive model for describing shear behaviour of woven reinforced thermoplastic composites, Composites Part A: Applied Science and Manufacturing 80 (2016) 194–203. https://doi.org/10.1016/j.compositesa.2015.10.028

[7] F. Schäfer, H.O. Werner, F. Henning, L. Kärger, A hyperelastic material model considering biaxial coupling of tension–compression and shear for the forming simulation of woven fabrics, Composites Part A: Applied Science and Manufacturing 165 (2023). https://doi.org/10.1016/j.compositesa.2022.107323

[8] Y. Gong, D. Yan, Y. Yao, R. Wei, H. Hu, P. Xu, X. Peng, An Anisotropic Hyperelastic Constitutive Model with Tension–Shear Coupling for Woven Composite Reinforcements, Int. J. Appl. Mechanics 09 (2017). https://doi.org/10.1142/S1758825117500831

[9] Y. Yao, X. Huang, X. Peng, P. Liu, G. Youkun, An anisotropic hyperelastic constitutive model for plain weave fabric considering biaxial tension coupling, Textile Research Journal 89 (2019) 434–444. https://doi.org/10.1177/0040517517748495

[10] P. Böhler, F. Härtel, P. Middendorf, Identification of Forming Limits for Unidirectional Carbon Textiles in Reality and Mesoscopic Simulation, Key Engineering Materials 554–557 (2013) 423–432. https://doi.org/10.4028/www.scientific.net/KEM.554-557.423

[11] S. Lomov, D. Ivanov, I. Verpoest, M. Zako, T. Kurashiki, H. Nakai, S. Hirosawa, Meso-FE modelling of textile composites: Road map, data flow and algorithms, Composites Science and Technology 67 (2007) 1870–1891. https://doi.org/10.1016/j.compscitech.2006.10.017

[12] J. Sirtautas, A.K. Pickett, P. Lépicier, A mesoscopic model for coupled drape-infusion simulation of biaxial Non-Crimp Fabric, Composites Part B: Engineering 47 (2013) 48–57. https://doi.org/10.1016/j.compositesb.2012.09.088

[13] G. Creech, A. Pickett, Meso-modelling of Non-Crimp Fabric composites for coupled drape and failure analysis, Journal of Materials Science 41 (2006) 6725–6736. https://doi.org/10.1007/s10853-006-0213-6

[14] F.J. Schirmaier, D. Dörr, F. Henning, L. Kärger, A macroscopic approach to simulate the forming behaviour of stitched unidirectional non-crimp fabrics (UD-NCF), Composites Part A: Applied Science and Manufacturing 102 (2017) 322–335. https://doi.org/10.1016/j.compositesa.2017.08.009

[15] B. Schäfer, S. Haas, P. Boisse, L. Kärger, Investigation of the Membrane Behavior of UD-NCF in Macroscopic Forming Simulations, Key Engineering Materials 926 (2022) 1413–1422. https://doi.org/10.4028/p-2977b4

[16] V.N. Khiêm, H. Krieger, M. Itskov, T. Gries, S.E. Stapleton, An averaging based hyperelastic modeling and experimental analysis of non-crimp fabrics, International Journal of Solids and Structures (2016). https://doi.org/10.1016/j.ijsolstr.2016.12.018

[17] B. Schäfer, D. Dörr, R. Zheng, N. Naouar, L. Kärger, A hyperelastic approach for modeling the membrane behavior in finite element forming simulation of unidirectional non-crimp fabrics (UD-NCF), Composites Part A: Applied Science and Manufacturing 185 (2024) 108359. https://doi.org/10.1016/j.compositesa.2024.108359

[18] B. Schäfer, Macroscopic forming simulation of unidirectional non-crimp fabrics: Hyperelastic material modeling and 3D-solid-shell approach, Doctoral Thesis, KIT, Karlsruhe, 2024. https://doi.org/10.5445/IR/1000170739

[19] B. Schäfer, D. Dörr, N. Naouar, J.P. Wank, L. Kärger, Capabilities and limitations of pure-shear based macroscopic forming simulations for 0°/90° biaxial non-crimp fabrics, in: Material Forming, 2025.

[20] N. Hamila, P. Boisse, Locking in simulation of composite reinforcement deformations. Analysis and treatment, Composites Part A: Applied Science and Manufacturing 53 (2013) 109–117. https://doi.org/10.1016/j.compositesa.2013.06.001

[21] D. Dörr, F.J. Schirmaier, F. Henning, L. Kärger, A viscoelastic approach for modeling bending behavior in finite element forming simulation of continuously fiber reinforced composites, Composites Part A: Applied Science and Manufacturing 94 (2017) 113–123. https://doi.org/10.1016/j.compositesa.2016.11.027

[22] B. Schäfer, R. Zheng, N. Naouar, L. Kärger, Membrane behavior of uni- and bidirectional non-crimp fabrics in off-axis-tension tests, Int J Mater Form 16 (2023) 1–15. https://doi.org/10.1007/s12289-023-01792-x

[23] ASTM D1388-18: Standard Test Method for Determining the Flexural Stiffness of Medical Textiles, (2018). https://www.astm.org/f3260-18.html

[24] ASTM D1894-14: Standard Test Method for Static and Kinetic Coefficients of Friction of Plastic Film and Sheeting (Withdrawn 2023), (2023). https://www.astm.org/d1894-14.html

[25] SimuDrape: Add-on for Abaqus/CAE, SIMUTENCE GmbH. https://www.simutence.de/products/simudrape/